INTERNATIONAL JOURNAL FOR NUMERICAL METHODS IN FLUIDS
Int. J. Numer. Meth. Fluids 2016; **82**:839–857
Published online 18 May 2016 in Wiley Online Library (wileyonlinelibrary.com). DOI: 10.1002/fld.4243

Residual-based stabilization of the finite element approximation to the acoustic perturbation equations for low Mach number aeroacoustics

Oriol Guasch[1,*,†], Patricia Sánchez-Martín[1], Arnau Pont[2], Joan Baiges[2] and Ramon Codina[2]

[1]*GTM - Grup de recerca en Tecnologies Mèdia, La Salle, Universitat Ramon Llull, C/ Quatre Camins 2, 08022 Barcelona, Catalonia*
[2]*Universitat Politècnica de Catalunya, C/ Jordi Girona 1-3, Edifici C1, 08034 Barcelona, Catalonia*

SUMMARY

The acoustic perturbation equations (APE) are suitable to predict aerodynamic noise in the presence of a non-uniform mean flow. As for any hybrid computational aeroacoustics approach, a first computational fluid dynamics simulation is carried out from which the mean flow characteristics and acoustic sources are obtained. In a second step, the APE are solved to get the acoustic pressure and particle velocity fields. However, resorting to the finite element method (FEM) for that purpose is not straightforward. Whereas mixed finite elements satisfying an appropriate inf–sup compatibility condition can be built in the case of no mean flow, that is, for the standard wave equation in mixed form, these are difficult to implement and their good performance is yet to be checked for more complex wave operators. As a consequence, strong simplifying assumptions are usually considered when solving the APE with FEM. It is possible to avoid them by resorting to stabilized formulations. In this work, a residual-based stabilized FEM is presented for the APE at low Mach numbers, which allows one to deal with the APE convective and reaction terms in its full extent. The key of the approach resides in the design of the matrix of stabilization parameters. The performance of the formulation and the contributions of the different terms in the equations are tested for an acoustic pulse propagating in sheared-solenoidal mean flow, and for the aeolian tone generated by flow past a two-dimensional cylinder. Copyright © 2016 John Wiley & Sons, Ltd.

Received 29 July 2015; Revised 6 April 2016; Accepted 9 April 2016

KEY WORDS: acoustics; aeroacoustics; stabilized FEM; variational multiscale (VMS); finite element; subsonic

1. INTRODUCTION

In this work, a stabilized finite element method (FEM) is proposed to solve the acoustic perturbation equations (APE). These equations can account for aerodynamic sound propagation in areas with non-uniform mean flow. In particular, we will herein focus on the low Mach number APE in [1], which are derived after source filtering the linearized Euler equations (LEE) to get rid of the vorticity and entropy modes while leaving the acoustic ones.

The APE constitute a particular case of the so-called hybrid methods in computational aeroacoustics (CAA). These separate the computation of aerodynamic sound into two steps. In the first one, a computational fluid dynamics (CFD) simulation is carried out to obtain the acoustic source terms from the aerodynamic velocity and pressure fields. In the second one, the source terms are input into an acoustic wave operator. The latter can directly be, for example, the standard linear wave equation

*Correspondence to: Oriol Guasch, GTM - Grup de recerca en Tecnologies Mèdia, La Salle, Universitat Ramon Llull, C/ Quatre Camins 2, 08022 Barcelona, Catalonia.
†E-mail: oguasch@salle.url.edu

in irreducible or mixed form, their convective counterparts or more complex operators like the ones involved in the LEE.

The best known hybrid approaches are those in the category of acoustic analogies, being Lighthill's the most celebrated one [2]. Lighthill's analogy states the problem of aerodynamic sound radiation into a quiescent medium as that of noise radiated by a distribution of quadrupoles in free space. For low Mach number flows, Lighthill approximates the source of sound by the double divergence of the Reynolds tensor, which is built from the products of the components of the aerodynamic velocity vector. Other analogies place their emphasis on the role of vorticity in the generation of sound [3–5]. Besides, it should be remarked that the influence of rigid bodies within the flow on noise radiation was considered since the birth of acoustic analogies ([6]) and later generalized to flexible bodies in [7].

As long as one aims to compute aerodynamic sound propagation in nonquiescent flow areas, convective and refraction effects have to be extracted from the acoustic source term and included in the wave operator (e.g. [8]). This led to the development of more sophisticated analogies (e.g. [9, 10]) and to alternatives such as the linearized Euler equations (LEE) [11] or resorting to perturbation equations [1, 12]. As mentioned earlier, in this work, we will attempt at solving a low Mach number formulation of the APE in [1] using FEM. Refraction effects will be neglected for simplicity.

The computation of aerodynamic sound in the second step of a hybrid CAA approach is often performed by resorting to integral formulations, though FEM is also common if the acoustic waves are to be computed at distances not too far from the source region. Most aeroacoustic FEM works to date have dealt with Lighthill's acoustic analogy, [13–16], yet convection effects have also been taken into account. In [17], the convective Helmholtz equation flow was considered, while a mixed convection wave equation with uniform mean flow was presented in [18] as a simplification of the second variant of the APE in [1].

The numerical difficulties associated to the FEM solution of the various wave operators involved in CAA are of a very different nature. Whereas for the standard linear wave equation for the acoustic pressure most efforts are placed on the time discretization schemes, given that the spatial discretization presents no serious difficulties (the Laplacian is a well-behaved operator), this is not the case for its Fourier transform, the Helmholtz equation. The latter may become nonpositive definite for large wavenumbers, and the standard Galerkin FEM approach fails to solve it. A large amount of stabilization strategies have been devised to prevent the pollution error associated to the Helmholtz equation [19]. With regard to mixed formulations like the APE, which involve both, the acoustic pressure and the acoustic particle velocity, the situation becomes more intricate. In the case of no convection, the APE simply reduces to the wave equation in mixed form. The variational formulation of the latter has to satisfy a compatibility inf–sup condition for the problem to be well posed, which is not inherited by the standard Galerkin FEM approach to it. It therefore becomes necessary to work with finite elements having different interpolations for the acoustic pressure and velocity fields to avoid the appearance of spurious oscillations in the numerical solution [20–22]. An alternative to circumvent the discrete inf–sup condition and consider the same interpolation fields for the acoustic pressure and velocity is that of resorting to stabilization strategies, such as the residual-based multiscale methods [23–25]. These were applied to the mixed wave equation in [26]. It was proved in [27] that the solution to the problem is then bounded by the data in an energy norm that involves all additional stabilization terms.

The situation worsens when one considers the presence of a mean flow. As far as the authors know, it has not been checked yet whether the tailored finite elements for the mixed wave equation could perform well in the presence of convection. Even if this was the case, their implementation is not an easy task. Stabilized FEM offers a way out to these problems. A first simplification to the APE is that of assuming a uniform mean flow so that they reduce to the convective mixed wave equation. As previously commented, this occurrence was addressed in [18], where a stabilizing flux term (as in the discontinuous Galerkin method) and a penalization term were incorporated in the formulation. However, in the case of a non-uniform mean flow, not only the convective terms in the APE become more complex, but one also has to deal with a reaction term. With regard to the former, analogous non-uniform convective terms appear in the linearized modified Boussinesq equation for shallow waters. The Galerkin FEM approach to it exhibits high-frequency oscillations [28, 29] that

DOI: 10.1002/fld

can be overcome by resorting to stabilization strategies [30, 31]. The same type of instabilities are found when setting the wave equation in mixed form in an arbitrary Lagrangian–Eulerian (ALE) frame of reference, to deal with wave propagation in moving domains [32]. Stabilization strategies have been also applied to the LEE. In particular, the discontinuous Galerkin and the stream upwind Petrov–Galerkin (SUPG) approaches were tested in [33] to suppress the artificial growth of the Kelvin–Helmholtz instabilities in the LEE (these instabilities are limited in real flows by nonlinear effects). Furthermore, the algebraic subgrid scale method in [17] was used to stabilize the standard Galerkin FEM approach to the LEE in [34].

The contributions of this work are as follows. First, a residual-based stabilized FEM is developed to solve a simplified version of the second variant of the APE ([1, 18]), which includes the effects of non-uniform convection and of the reaction term due to the mean velocity gradient. As far as the authors know, neither these effects had been taken into account in previous FEM approaches to the APE, nor residual-based FEM methods have been applied to them. Besides, the implemented stabilization strategy relies on splitting the problem unknowns into large scales that can be resolved by the computational mesh, and small scales whose effects onto the large scales have to be modelled. Its main advantage is that equal degree of interpolation can be used for the acoustic pressure and particle velocity fields, yet the key for the good performance of the method depends upon the design of a proper matrix of stabilization parameters, which constitutes the second main goal of the work. This is achieved through a Fourier analysis of the subscale equation following the lines in [26, 31, 32]. Finally, the importance of the various terms in the analyzed APE system is highlighted by means of some numerical examples. The latter reveal that neglecting some of the terms to simplify the equations may result in significant deviations in the wavefronts of the predicted aerodynamic sound.

The paper is organized as follows. In Section 2, we disclose the APE, set them in matrix form and work out their variational formulation. In Section 3, we proceed to discretization. The residual-based stabilized FEM approach is presented, and the derivation of the matrix of stabilization parameters is exposed in detail. The fully discretized numerical scheme in time and space close the section. Two numerical examples are finally given in Section 4. These consist of two benchmark tests dealing with the wavefront propagation in a solenoidal sheared mean flow and with the generation of an aeolian tone by flow past a two-dimensional cylinder.

2. PROBLEM STATEMENT

2.1. An acoustic perturbation equation for low Mach numbers

Our starting point will be the APE (53)–(55) derived in [1], in the particular case of only considering vortex sound for low Mach numbers and neglecting the linear coupling between acoustic and vorticity modes. These equations read

$$\partial_t \rho' + \nabla \cdot \left(\rho' \bar{\boldsymbol{u}} + \bar{\rho} \boldsymbol{u}^a\right) = 0, \tag{1a}$$

$$\partial_t \boldsymbol{u}^a + \nabla(\bar{\boldsymbol{u}} \cdot \boldsymbol{u}^a) + \nabla\left(\frac{p^a}{\bar{\rho}}\right) = \boldsymbol{0}, \tag{1b}$$

$$\partial_t p^a - \bar{c}^2 \partial_t \rho' = -\partial_t p^h, \tag{1c}$$

and are obtained from manipulation of the linearized Euler equations for the enthalpy and velocity fields (the reader is referred to [1] for details). ∂_t stands for the first order time derivative, and $\bar{c}$ denotes the speed of sound. The aforementioned equations are based on the following decompositions for the compressible velocity $\boldsymbol{u}$, pressure p and density ρ,

$$\boldsymbol{u} = \bar{\boldsymbol{u}} + \boldsymbol{u}' \quad \text{with} \quad \boldsymbol{u}' := \boldsymbol{u}^h + \boldsymbol{u}^a, \tag{2a}$$

$$p = \bar{p} + p' \quad \text{with} \quad p' := p^h + p^a, \tag{2b}$$

$$\rho = \bar{\rho} + \rho' \quad \text{with} \quad \rho' := \rho^h + \rho^a. \tag{2c}$$

DOI: 10.1002/fld

In (1)–(2) an overbar indicates a time averaged mean quantity, that is, $\overline{g(\boldsymbol{x})} := \lim_{T\to\infty}(1/T)\int_{t_0}^{t_0+T} g(\boldsymbol{x},t)dt$, with t_0 standing for the initial time of the averaging process and T for its total duration. The mean values are independent of t_0 once the initial transients of a simulation/measurement have been surpassed. Likewise, a prime $g(\boldsymbol{x},t)'$ denotes a perturbation from the mean value. The velocity fluctuation $\boldsymbol{u}'$ in (2a) becomes split into two components, a hydrodynamic solenoidal perturbation $\boldsymbol{u}^h$ and an irrotational acoustic perturbation $\boldsymbol{u}^a$. Similarly, the pressure and density fluctuations p' and ρ' in (2b) and (2c) consist of two terms, a hydrodynamic component p^h and ρ^h responsible for the production of pseudo-sound and an acoustic component p^a and ρ^a that will propagate as acoustic waves outwards the source region.

Equation 1 can be further simplified assuming that neither the time averaged sound speed nor the time averaged density have a spatial dependence, that is, $\bar{c} \equiv c_0$ and $\bar{\rho} \equiv \rho_0$. Moreover and given that we are dealing with low Mach number flows, we can resort to an incompressible computational fluid dynamics (CFD) simulation to compute the mean hydrodynamic velocity $\bar{\boldsymbol{u}}$ and the hydrodynamic pressure p^h. In such situation, we get $\nabla\cdot\bar{\boldsymbol{u}} = 0$ and assuming $p' = c_0^2\rho'$, Equation 1 simplifies to

$$\frac{1}{\rho_0 c_0^2}\partial_t p^a + \frac{1}{\rho_0 c_0^2}\,\bar{\boldsymbol{u}}\cdot\nabla p^a + \nabla\cdot\boldsymbol{u}^a = -\frac{1}{\rho_0 c_0^2}\partial_t p^h - \frac{1}{\rho_0 c_0^2}\bar{\boldsymbol{u}}\cdot\nabla p^h, \tag{3a}$$

$$\rho_0\partial_t\boldsymbol{u}^a + \rho_0\,\bar{\boldsymbol{u}}\cdot\nabla\boldsymbol{u}^a + \nabla p^a + \rho_0\,\boldsymbol{u}^a\cdot\nabla\bar{\boldsymbol{u}} = \boldsymbol{0}. \tag{3b}$$

Equation 3 constitutes the simplification proposed in [18] for the APE variant 2 in [1]. It only involves the acoustic pressure and acoustic particle velocity as the problem unknowns. In the present work, we will extend the analysis in [18] by considering non-uniform mean velocity flows. Notice that the reaction term $\rho_0\,\boldsymbol{u}^a\cdot\nabla\bar{\boldsymbol{u}}$ does not vanish in such cases.

2.2. *Differential matrix problem and variational formulation*

It is possible to rewrite Equations (3a) and (3b) in matrix form for convenience as

$$\boldsymbol{\mu}\partial_t\boldsymbol{U} + \boldsymbol{A}_i\partial_i\boldsymbol{U} + \boldsymbol{S}\,\boldsymbol{U} = \boldsymbol{F}, \tag{4}$$

where the summation convention over repeated indexes is assumed hereinafter. The index i will run from 1 to the number of spatial dimensions with ∂_i standing for the first order spatial derivatives. The following vector and matrix identifications have been made

$$\boldsymbol{U} = \begin{pmatrix} p^a \\ u_1^a \\ u_2^a \\ u_3^a \end{pmatrix}, \boldsymbol{F} = \begin{pmatrix} Q \\ f_1 \\ f_2 \\ f_3 \end{pmatrix}, \boldsymbol{\mu} = \begin{pmatrix} \mu_p & 0 & 0 & 0 \\ 0 & \mu_{\boldsymbol{u}} & 0 & 0 \\ 0 & 0 & \mu_{\boldsymbol{u}} & 0 \\ 0 & 0 & 0 & \mu_{\boldsymbol{u}} \end{pmatrix}, \boldsymbol{A}_1 = \begin{pmatrix} \mu_p\bar{u}_1 & 1 & 0 & 0 \\ 1 & \mu_{\boldsymbol{u}}\bar{u}_1 & 0 & 0 \\ 0 & 0 & \mu_{\boldsymbol{u}}\bar{u}_1 & 0 \\ 0 & 0 & 0 & \mu_{\boldsymbol{u}}\bar{u}_1 \end{pmatrix},$$

$$\boldsymbol{A}_2 = \begin{pmatrix} \mu_p\bar{u}_2 & 0 & 1 & 0 \\ 0 & \mu_{\boldsymbol{u}}\bar{u}_2 & 0 & 0 \\ 1 & 0 & \mu_{\boldsymbol{u}}\bar{u}_2 & 0 \\ 0 & 0 & 0 & \mu_{\boldsymbol{u}}\bar{u}_2 \end{pmatrix}, \boldsymbol{A}_3 = \begin{pmatrix} \mu_p\bar{u}_3 & 0 & 0 & 1 \\ 0 & \mu_{\boldsymbol{u}}\bar{u}_3 & 0 & 0 \\ 0 & 0 & \mu_{\boldsymbol{u}}\bar{u}_3 & 0 \\ 1 & 0 & 0 & \mu_{\boldsymbol{u}}\bar{u}_3 \end{pmatrix},$$

$$\boldsymbol{S} = \begin{pmatrix} 0 & 0 & 0 & 0 \\ 0 & \mu_{\boldsymbol{u}}\partial_1\bar{u}_1 & \mu_{\boldsymbol{u}}\partial_2\bar{u}_1 & \mu_{\boldsymbol{u}}\partial_3\bar{u}_1 \\ 0 & \mu_{\boldsymbol{u}}\partial_1\bar{u}_2 & \mu_{\boldsymbol{u}}\partial_2\bar{u}_2 & \mu_{\boldsymbol{u}}\partial_3\bar{u}_2 \\ 0 & \mu_{\boldsymbol{u}}\partial_1\bar{u}_3 & \mu_{\boldsymbol{u}}\partial_2\bar{u}_3 & \mu_{\boldsymbol{u}}\partial_3\bar{u}_3 \end{pmatrix}. \tag{5}$$

The parameters $\mu_p \equiv (\rho_0 c_0^2)^{-1}$ and $\mu_{\boldsymbol{u}} \equiv \rho_0$ satisfying $c_0 = (\mu_p\mu_{\boldsymbol{u}})^{-1/2}$ in (5) have been introduced to ease the notation and $\bar{u}_i$, $i = 1,2,3$, designate the components of the time-averaged mean velocity vector. Note also that, for completeness, we have included the possibility of an external force acting on the momentum equation by means of the components f_i.

Problem (4) is to be solved in a computational domain Ω whose boundary $\partial\Omega$ can be considered to be made from the union of two disjoint sets: Γ_p where we will prescribe the acoustic pressure and

DOI: 10.1002/fld

$\Gamma_{\boldsymbol{u}}$ where the normal component of the acoustic particle velocity is to be imposed. For simplicity, we shall take homogeneous Dirichlet conditions on them in the forthcoming expressions, that is, $p^a = 0$ on $\Gamma_p,\ t > 0$ and $\boldsymbol{u}^a \cdot \boldsymbol{n} = 0$ on $\Gamma_{\boldsymbol{u}},\ t > 0$, with $\boldsymbol{n}$ standing for the outward normal of the domain's boundary. Equation 4 needs also to be suplemmented with initial conditions $p^a(\boldsymbol{x}, 0) = p_0^a(\boldsymbol{x})$ and $\boldsymbol{u}^a(\boldsymbol{x}, 0) = \boldsymbol{u}_0^a(\boldsymbol{x})$ in Ω.

Additionally, let us introduce the functional spaces $V_p(\Omega) = \{q \in H^1(\Omega) | \bar{\boldsymbol{u}} \cdot \nabla q \in L^2(\Omega), q = 0 \text{ on } \Gamma_p\}$ and $\boldsymbol{V}_{\boldsymbol{u}}(\Omega) = \{\boldsymbol{v} \in \boldsymbol{L}^2(\Omega) | \nabla \cdot \boldsymbol{v} \in L^2(\Omega), \bar{\boldsymbol{u}} \cdot \nabla \boldsymbol{v} \in \boldsymbol{L}^2(\Omega), \boldsymbol{v} \cdot \boldsymbol{n} = 0 \text{ on } \Gamma_{\boldsymbol{u}}\}$ and use (f, g) to denote the integral of the product of two arbitrary functions f and g, that is, $(f, g) := \int_\Omega f g \, d\Omega$. Analogously, for vector valued functions, we will have $(\boldsymbol{f}, \boldsymbol{g}) := \int_\Omega \boldsymbol{f}^\top \boldsymbol{g} \, d\Omega$. Next, consider a test function q for the acoustic pressure and $\boldsymbol{v}$ for the acoustic velocity. The weak form of (4) is found multiplying it by a vector test function $\boldsymbol{V} \equiv [q, \boldsymbol{v}]^\top$ and integrating over the computational domain Ω. Defining the spaces $\mathcal{L}(\Omega) \equiv L^2(\Omega) \times \boldsymbol{L}^2(\Omega)$ and $\mathcal{V}(\Omega) \equiv V_p(\Omega) \times \boldsymbol{V}_{\boldsymbol{u}}(\Omega)$, the problem becomes that of finding $\boldsymbol{U} \equiv [p^a, \boldsymbol{u}^a]^\top \in \boldsymbol{C}^1([0, T], \mathcal{L}(\Omega)) \cap \boldsymbol{C}^0([0, T], \mathcal{V}(\Omega))$ such that

$$(\boldsymbol{\mu} \partial_t \boldsymbol{U}, \boldsymbol{V}) + (\boldsymbol{A}_i \partial_i \boldsymbol{U}, \boldsymbol{V}) + (\boldsymbol{S}\boldsymbol{U}, \boldsymbol{V}) = (\boldsymbol{F}, \boldsymbol{V}) \quad \forall \boldsymbol{V} \in \mathcal{V}(\Omega). \tag{6}$$

3. NUMERICAL APPROXIMATION

3.1. Residual-based stabilized finite element method

The standard discretized conforming Galerkin FEM approach to solve problem (6) aims at finding a finite element solution $\boldsymbol{U}_h \in \boldsymbol{C}^1([0, T], \mathcal{L}_h(\Omega) \subset \mathcal{L}(\Omega)) \cap \boldsymbol{C}^0([0, T], \mathcal{V}_h(\Omega) \subset \mathcal{V}(\Omega))$ such that

$$(\boldsymbol{\mu} \partial_t \boldsymbol{U}_h, \boldsymbol{V}_h) + (\boldsymbol{A}_i \partial_i \boldsymbol{U}_h, \boldsymbol{V}_h) + (\boldsymbol{S}\boldsymbol{U}_h, \boldsymbol{V}_h) = (\boldsymbol{F}, \boldsymbol{V}_h) \quad \forall \boldsymbol{V}_h \in \mathcal{V}_h(\Omega). \tag{7}$$

Here, $\mathcal{L}_h(\Omega)$, $\mathcal{V}_h(\Omega)$ represent finite dimensional spaces built from a finite element partition $\{\Omega_e\}$ of Ω. The index e ranges from 1 to the total number of elements n_{el} in the computational mesh. However, the Galerkin FEM formulation (7) is known to suffer from numerical instabilities which can be overcome by resorting to a variational multiscale stabilization approach. The latter basically consists in splitting the exact solution $\boldsymbol{U}$ into a large component $\boldsymbol{U}_h$ that can be captured by the finite element computational mesh, plus a small component $\boldsymbol{U}'$, which cannot be resolved by the mesh. $\boldsymbol{U}'$ is usually referred to as the subscale. The effects of the subscales onto the large scales have to be modelled. The procedure to do so gives rise to different stabilization methods.

Substituting $\boldsymbol{U} = \boldsymbol{U}_h + \boldsymbol{U}'$ into (6) results in two equations. The first one governs the dynamics of the large scales and is given by

$$(\boldsymbol{\mu} \partial_t \boldsymbol{U}_h, \boldsymbol{V}_h) + (\boldsymbol{\mu} \partial_t \boldsymbol{U}', \boldsymbol{V}_h) + (\boldsymbol{A}_i \partial_i \boldsymbol{U}_h, \boldsymbol{V}_h) + (\boldsymbol{A}_i \partial_i \boldsymbol{U}', \boldsymbol{V}_h) + (\boldsymbol{S}\boldsymbol{U}_h, \boldsymbol{V}_h) + (\boldsymbol{S}\boldsymbol{U}', \boldsymbol{V}_h) = (\boldsymbol{F}, \boldsymbol{V}_h). \tag{8}$$

To better appreciate the influence of the subscales in the large scale equation, we can integrate the convective term by parts presuming the subscales to be local and vanish at the inter-element boundaries. This is not a strong assumption given that no exact values can be found for the subscales; only their mean effects onto the large scales can be computed. Furthermore, we will assume the subscales to be quasi-static, that is, $\partial_t \boldsymbol{U}' \approx \boldsymbol{0}$. This hypothesis has proven valuable in previous stabilization works involving wave propagation phenomena; see [14, 17, 26, 31, 32]. On the other hand, the implementation of time evolving dynamic subscales has been considered, for example, in coupled problems involving the incompressible Navier–Stoles equations [35–37]. However, for simplicity, dynamic subscales will not be taken into account in this first work on stabilized FEM for the APE that being left for future developments. All this leads to the following expression for Equation 8,

$$\begin{aligned} &(\boldsymbol{\mu} \partial_t \boldsymbol{U}_h, \boldsymbol{V}_h) + (\boldsymbol{A}_i \partial_i \boldsymbol{U}_h, \boldsymbol{V}_h) + (\boldsymbol{S}\boldsymbol{U}_h, \boldsymbol{V}_h) \\ &- (\boldsymbol{U}', \boldsymbol{A}_i^\top \partial_i \boldsymbol{V}_h) - (\boldsymbol{U}', [\partial_i \boldsymbol{A}_i^\top] \boldsymbol{V}_h) + (\boldsymbol{U}', \boldsymbol{S}^\top \boldsymbol{V}_h) = (\boldsymbol{F}, \boldsymbol{V}_h). \end{aligned} \tag{9}$$

DOI: 10.1002/fld

Notice that the first line in (9) contains the terms of the standard Galerkin approach in (7), whereas the second line discloses the subscale stabilization terms. The term $(\boldsymbol{U}', [\partial_i \boldsymbol{A}_i^\top]\boldsymbol{V}_h)$ in the second line plays the role of an additional reaction weighted by the subscales, yet as seen from (5), this term automatically vanishes because we are considering solenoidal mean flows.

On the other hand, the second equation driving the dynamics of $\boldsymbol{U}'$ has the expression

$$(\boldsymbol{\mu}\partial_t \boldsymbol{U}_h, \boldsymbol{V}') + (\boldsymbol{A}_i\partial_i \boldsymbol{U}_h, \boldsymbol{V}') + (\boldsymbol{A}_i\partial_i \boldsymbol{U}', \boldsymbol{V}') + (\boldsymbol{S}\boldsymbol{U}_h, \boldsymbol{V}') + (\boldsymbol{S}\boldsymbol{U}', \boldsymbol{V}') = (\boldsymbol{F}, \boldsymbol{V}'), \quad (10)$$

which corresponds to the L^2-projection of $\boldsymbol{\mu}\partial_t \boldsymbol{U}_h + \boldsymbol{A}_i\partial_i \boldsymbol{U}_h + \boldsymbol{A}_i\partial_i \boldsymbol{U}' + \boldsymbol{S}\boldsymbol{U}_h + \boldsymbol{S}\boldsymbol{U}' = \boldsymbol{F}$ onto the space of subscales. If we use $\mathcal{P}$ to denote this projection, (10) can be rewritten as

$$\mathcal{P}(\boldsymbol{A}_i\partial_i \boldsymbol{U}' + \boldsymbol{S}\boldsymbol{U}') = \mathcal{P}[\boldsymbol{F} - (\boldsymbol{\mu}\partial_t \boldsymbol{U}_h + \boldsymbol{A}_i\partial_i \boldsymbol{U}_h + \boldsymbol{S}\boldsymbol{U}_h)] =: \boldsymbol{R}_h, \quad (11)$$

where the residual $\boldsymbol{R}_h$ of the finite element approximation onto the subscale space has been introduced. The goal of the residual-based stabilization approaches is to find an approximate solution to (11), which yields an expression for $\boldsymbol{U}'$ that could be substituted in (9) resulting in enhanced stabilization properties.

A standard option consists in taking the subscales proportional to the residual, that is, $\boldsymbol{U}' = \boldsymbol{\tau}\boldsymbol{R}_h$, which in our case, is analogous to saying that $\mathcal{P}(\boldsymbol{A}_i\partial_i \boldsymbol{U}' + \boldsymbol{S}\boldsymbol{U}') \approx \boldsymbol{\tau}^{-1}\boldsymbol{U}'$; see [26, 31, 32]. Here, $\boldsymbol{\tau}$ stands for a symmetric, positive-definite matrix of stabilization parameters that has to be determined. Once this has been carried out, $\boldsymbol{U}' = \boldsymbol{\tau}\boldsymbol{R}_h$ can be substituted into the large scale equation (9) that becomes

$$\begin{aligned}&(\boldsymbol{\mu}\partial_t \boldsymbol{U}_h, \boldsymbol{V}_h) + (\boldsymbol{A}_i\partial_i \boldsymbol{U}_h, \boldsymbol{V}_h) + (\boldsymbol{S}\boldsymbol{U}_h, \boldsymbol{V}_h)\\ &\quad + (\boldsymbol{\tau}\mathcal{P}[\boldsymbol{F} - (\boldsymbol{\mu}\partial_t \boldsymbol{U}_h + \boldsymbol{A}_i\partial_i \boldsymbol{U}_h + \boldsymbol{S}\boldsymbol{U}_h)], -\boldsymbol{A}_i\partial_i \boldsymbol{V}_h + \boldsymbol{S}^\top \boldsymbol{V}_h) = (\boldsymbol{F}, \boldsymbol{V}_h).\end{aligned} \quad (12)$$

Note that we have used the fact that the convective matrices $\boldsymbol{A}_i$ are symmetric in the aforementioned expression. It is also to be remarked that the matrix of stabilization parameters $\boldsymbol{\tau}$ has to be computed elementwise. With regard to the projection operator, $\mathcal{P}$, different options exist. In the more classical algebraic subgrid scale formulation, the projection is taken as the identity matrix over the space of finite element residuals, that is, $\mathcal{P} = \boldsymbol{I}$. Alternatively, in the orthogonal subgrid scale method the subscales are assumed to be orthogonal to the finite element space and consequently, $\mathcal{P} = \boldsymbol{I} - \Pi_h$, with Π_h standing for the L^2-projection onto the former [25, 35].

3.2. Dimensional rescaling considerations

To complete the stabilized formulation in (12), the crucial step of finding an appropriate expression for the stabilization matrix $\boldsymbol{\tau}$ remains to be performed. However, before addressing such an issue some considerations are to be made concerning the scalar products in the variational formulations (5) and (12). The right hand side (RHS) of these equations involves products of the type $\boldsymbol{U}^\top \boldsymbol{F} = p^a Q + u_1^a f_1 + u_2^a f_2 + u_3^a f_3$ (5). If we use $[\cdot]$ to denote a dimensional group, it becomes necessary that $[p^a Q] = [u_i^a f_i]$. From the dimensions of the terms in the RHS of (3) it can readily be checked that $[p^a Q] = [u_i^a f_i] = MLT^{-3}$, with M, L and T standing for dimensions of mass, length and time, respectively. Yet, when deriving an appropriate expression for $\boldsymbol{\tau}$ in the next subsection, we will have to deal with products like $\boldsymbol{F}^\top \boldsymbol{F}$ or $\boldsymbol{U}^\top \boldsymbol{U}$, which are not dimensionally well defined. For instance, $\boldsymbol{F}^\top \boldsymbol{F} = Q^2 + f_1^2 + f_2^2 + f_3^2$ but $[Q^2] \neq [f_i^2]$. Similarly, $\boldsymbol{U}^\top \boldsymbol{U} = p^{a\,2} + u_1^{a\,2} + u_2^{a\,2} + u_3^{a\,2}$ but again $[p^{a\,2}] \neq [u_i^{a\,2}]$. Consequently, and as quoted in [26, 31], it becomes necessary to rescale the original differential equations for these products to make sense.

This is tantamount to introducing the weighting matrix $\boldsymbol{M}$ [26],

$$\boldsymbol{M} = \begin{pmatrix} m_p & 0 & 0 & 0 \\ 0 & m_{\boldsymbol{u}} & 0 & 0 \\ 0 & 0 & m_{\boldsymbol{u}} & 0 \\ 0 & 0 & 0 & m_{\boldsymbol{u}} \end{pmatrix}, \quad m_p := \sqrt{\mu_{\boldsymbol{u}}/\mu_p} = \rho_0 c_0, \quad m_{\boldsymbol{u}} := \sqrt{\mu_p/\mu_{\boldsymbol{u}}} = \frac{1}{\rho_0 c_0}, \quad (13)$$

DOI: 10.1002/fld

to define the weighted scalar product $\boldsymbol{F}^\top \boldsymbol{M}\boldsymbol{F} \equiv |\boldsymbol{F}|^2_{\boldsymbol{M}}$, which can be shown to be dimensionally correct given that $[m_p Q^2] = \left[m_{\boldsymbol{u}} f_i^2\right] = ML^{-2}T^{-3}$. Analogously, the inverse of $\boldsymbol{M}$ can be used to correctly define the product $\boldsymbol{U}^\top \boldsymbol{M}^{-1}\boldsymbol{U} \equiv |\boldsymbol{U}|^2_{\boldsymbol{M}^{-1}}$. That is so because $\left[m_p^{-1} p^{a2}\right] = \left[m_{\boldsymbol{u}}^{-1} u_i^{a2}\right] = MT^{-3}$. Therefore, $\boldsymbol{M}$ and $\boldsymbol{M}^{-1}$ are the appropriate weighthing matrices to define products between any two force vectors $\boldsymbol{F}_1^\top \boldsymbol{M}\boldsymbol{F}_2$ and unknowns $\boldsymbol{U}_1^\top \boldsymbol{M}^{-1}\boldsymbol{U}_2$. We can also define an $\boldsymbol{M}$-weighted product between two arbitrary matrices $\boldsymbol{B}_1$ and $\boldsymbol{B}_2$ as $\boldsymbol{B}_1^\top \boldsymbol{M}\boldsymbol{B}_2$. The squared $\boldsymbol{M}$-pointwise norm of a matrix $\boldsymbol{B}$ will be given by $|\boldsymbol{B}|^2_{\boldsymbol{M}} = \sup\{\boldsymbol{X}^\top \boldsymbol{B}^\top \boldsymbol{M}\boldsymbol{B}\boldsymbol{X}\}$, $\forall \boldsymbol{X}; |\boldsymbol{X}|_{\boldsymbol{M}^{-1}} = 1$. For regular enough force vector functions, it is also possible to introduce the following vector function $\boldsymbol{M}$-weighted scalar products,

$$(\boldsymbol{U},\boldsymbol{F}) = \int_\Omega \boldsymbol{U}^\top \boldsymbol{F}\, d\Omega, (\boldsymbol{F}_1,\boldsymbol{F}_2)_{\boldsymbol{M}} := \int_\Omega \boldsymbol{F}_1^\top \boldsymbol{M}\boldsymbol{F}_2 d\Omega, (\boldsymbol{U}_1,\boldsymbol{U}_2)_{\boldsymbol{M}^{-1}} := \int_\Omega \boldsymbol{U}_1^\top \boldsymbol{M}^{-1}\boldsymbol{U}_2 d\Omega, \tag{14}$$

whose induced norms are designated by $\|\cdot\|$, $\|\cdot\|_{\boldsymbol{M}}$ and $\|\cdot\|_{\boldsymbol{M}^{-1}}$.

3.3. The matrix $\boldsymbol{\tau}$ of stabilization parameters

A fruitful way to derive an expression for the matrix of stabilization parameters $\boldsymbol{\tau}$ is from the spatial Fourier transform of the subscale equation (11). To that purpose, we shall assume that the mean flow velocity and its derivatives are smoothly varying in the size of a typical mesh element, Ω_e, so that the matrices $\boldsymbol{A}_i$ and $\boldsymbol{S}$ can be assumed constant within Ω_e. We can thus define the Fourier transform of an arbitrary function $\boldsymbol{f}$ within Ω_e as $\hat{\boldsymbol{f}}(\boldsymbol{k}) := \int_{\Omega_e} \boldsymbol{f}(\boldsymbol{x}) \exp[-i(\boldsymbol{k}\cdot\boldsymbol{x})/h] d\Omega_e$ (e.g. [25]). Hereafter, a hat symbol will stand for Fourier transformed quantities, and k_i will denote the ith component of the wavenumber adimensionalized by the characteristic mesh size h. Identifying the linear operator $\mathscr{L} := \boldsymbol{A}_i \partial_i + \boldsymbol{S}$, we can express Equation 11 in the wavenumber domain as,

$$\hat{\mathscr{L}}(\boldsymbol{k})\hat{\boldsymbol{U}}' = -\mathrm{i}\frac{1}{h} k_j \boldsymbol{A}_j \hat{\boldsymbol{U}}' + \boldsymbol{S}\hat{\boldsymbol{U}}' = \hat{\boldsymbol{R}}_h, \tag{15}$$

with squared $\boldsymbol{M}$-norm

$$\hat{\boldsymbol{U}}'^\top \hat{\mathscr{L}}(\boldsymbol{k})^\top \boldsymbol{M}\hat{\mathscr{L}}(\boldsymbol{k})\hat{\boldsymbol{U}}' = \hat{\boldsymbol{U}}'^\top \left(\frac{1}{h^2} k_l k_j \boldsymbol{A}_l^\top \boldsymbol{M}\boldsymbol{A}_j + 2\frac{\mathrm{i}}{h} k_l [\boldsymbol{A}_l \boldsymbol{M}\boldsymbol{S}]_A + \boldsymbol{S}^\top \boldsymbol{M}\boldsymbol{S}\right)\hat{\boldsymbol{U}}' = \hat{\boldsymbol{R}}_h^\top \boldsymbol{M}\hat{\boldsymbol{R}}_h. \tag{16}$$

Here, $[\boldsymbol{A}_l \boldsymbol{M}\boldsymbol{S}]_A$ stands for the skew-symmetric part of $\boldsymbol{A}_l^\top \boldsymbol{M}\boldsymbol{S}$. The induced norm for the residual (15) fulfils

$$\begin{aligned}
\|\hat{\boldsymbol{R}}_h\|^2_{\boldsymbol{M}} &= \int \left|\hat{\boldsymbol{R}}_h\right|^2_{\boldsymbol{M}} d\boldsymbol{k} = \int \left|\hat{\mathscr{L}}(\boldsymbol{k})\hat{\boldsymbol{U}}'\right|^2_{\boldsymbol{M}} d\boldsymbol{k} \leqslant \int \left|\hat{\mathscr{L}}(\boldsymbol{k})\right|^2_{\boldsymbol{M}} \left|\hat{\boldsymbol{U}}'\right|^2_{\boldsymbol{M}^{-1}} d\boldsymbol{k} \\
&= |\hat{\mathscr{L}}(\boldsymbol{k}^0)|^2_{\boldsymbol{M}} \int |\hat{\boldsymbol{U}}'|^2_{\boldsymbol{M}^{-1}} d\boldsymbol{k} = |\hat{\mathscr{L}}(\boldsymbol{k}^0)|^2_{\boldsymbol{M}} \left\|\hat{\boldsymbol{U}}'\right\|^2_{\boldsymbol{M}^{-1}} \\
&= \rho(\hat{\mathscr{L}}(\boldsymbol{k}^0)^\top \boldsymbol{M}\hat{\mathscr{L}}(\boldsymbol{k}^0)) \left\|\hat{\boldsymbol{U}}'\right\|^2_{\boldsymbol{M}^{-1}} \\
&\leqslant \left[\rho\left(\frac{1}{h^2} k_l^0 k_j^0 \boldsymbol{A}_l^\top \boldsymbol{M}\boldsymbol{A}_j\right) + \rho\left(2\frac{\mathrm{i}}{h} k_l^0 [\boldsymbol{A}_l \boldsymbol{M}\boldsymbol{S}]_A\right) + \rho(\boldsymbol{S}^\top \boldsymbol{M}\boldsymbol{S})\right] \left\|\hat{\boldsymbol{U}}'\right\|^2_{\boldsymbol{M}^{-1}},
\end{aligned} \tag{17}$$

where the existence of a value of $\boldsymbol{k}^0$ that fulfils the equality in the second line is guaranteed by the mean value theorem. In the third line, we use the fact that the squared $\boldsymbol{M}$-pointwise norm of the operator $\mathscr{L}(\boldsymbol{k}^0)$ is given by its corresponding spectral radius $\rho(\hat{\mathscr{L}}(\boldsymbol{k}^0)^\top \boldsymbol{M}\hat{\mathscr{L}}(\boldsymbol{k}^0))$. Herein, we understand $\rho(\boldsymbol{B})$ to denote the spectral radius of an arbitrary matrix $\boldsymbol{B}$ arising from the solution of the generalized eigenvalue problem $\boldsymbol{B}\boldsymbol{U} = \lambda \boldsymbol{M}^{-1}\boldsymbol{U}$, λ being an eigenvalue. Finally, in the fourth line, we use the fact that the spectral radius of the sum of two matrices is bounded by the summation of the matrices' individual spectral radii. All spectral radii in that line will be shown to be real (note that $[\boldsymbol{A}_l \boldsymbol{M}\boldsymbol{S}]_A$ is totally skew-symmetric and therefore has imaginary eigenvalues).

DOI: 10.1002/fld

On the other hand, from the Fourier transform of the approximation for the subscales $\boldsymbol{U}' = \boldsymbol{\tau}\boldsymbol{R}_h$, we can get the bound

$$\left\|\hat{\boldsymbol{R}}_h\right\|^2_{\boldsymbol{M}} \leqslant \left|\boldsymbol{\tau}^{-1}\right|^2_{\boldsymbol{M}} \left\|\hat{\boldsymbol{U}}'\right\|^2_{\boldsymbol{M}^{-1}}. \tag{18}$$

The combination of (17) and (18) provides one way to find an expression for the stabilization matrix given that

$$\rho\left(\boldsymbol{\tau}^{-1}\boldsymbol{M}\boldsymbol{\tau}^{-1}\right) \leqslant \rho\left(\frac{1}{h^2}k_l^0 k_j^0 \boldsymbol{A}_l^\top \boldsymbol{M}\boldsymbol{A}_j\right) + \rho\left(2\frac{\mathrm{i}}{h}k_l^0[\boldsymbol{A}_l\boldsymbol{M}\boldsymbol{S}]_A\right) + \rho(\boldsymbol{S}^\top\boldsymbol{M}\boldsymbol{S}). \tag{19}$$

Bounds for the spectral radii in (19) are provided in Appendix A. From (19) and (A.14), it follows

$$\rho\left(\boldsymbol{\tau}^{-1}\boldsymbol{M}\boldsymbol{\tau}^{-1}\right) \leqslant \frac{1}{h^2}\left(C_1 + C_2 M\right)^2 + \frac{1}{h}\frac{C_3}{c_0}|\nabla\bar{\boldsymbol{u}}|_F + \frac{C_4}{c_0^2}|\nabla\bar{\boldsymbol{u}}|_F^2. \tag{20}$$

Taking into account that $|\nabla\bar{\boldsymbol{u}}| \sim \mathcal{O}(\bar{\boldsymbol{u}}/L) << \bar{\boldsymbol{u}}/h$, with L standing for a characteristic length of the domain, and redefining the constants in the expressions hereafter where appropriate, we can check that the bound on the $\boldsymbol{M}$-norm of the stabilization matrix behaves as

$$\rho\left(\boldsymbol{\tau}^{-1}\boldsymbol{M}\boldsymbol{\tau}^{-1}\right) << \frac{1}{h^2}[C_1 + C_2\mathcal{O}(M) + C_3\mathcal{O}(M^2)]. \tag{21}$$

Note that the discarded term involving M^2 in (A.8)–(A.9) would have given place to a term $\sim \mathcal{O}(M^3)$ in (21).

In order to get a simple expression for the stabilization matrix, we may take it to be diagonal, $\boldsymbol{\tau} = \mathrm{diag}(\tau_p, \tau_{\boldsymbol{u}}, \tau_{\boldsymbol{u}})$. Given that the scaling matrix $\boldsymbol{M}$ in (13) is also diagonal, it follows that

$$\mathrm{Spec}_{\boldsymbol{M}^{-1}}\left(\boldsymbol{\tau}^{-1}\boldsymbol{M}\boldsymbol{\tau}^{-1}\right) = \left\{\left(\frac{m_p}{\tau_p}\right)^2, \left(\frac{m_{\boldsymbol{u}}}{\tau_{\boldsymbol{u}}}\right)^2, \left(\frac{m_{\boldsymbol{u}}}{\tau_{\boldsymbol{u}}}\right)^2\right\}. \tag{22}$$

The maximum of these eigenvalues should behave as the RHS of (20) dictates in order to have control on all possible flow regimes. From (20) and the subsequent observation (21), it turns out that it is enough to have a term behaving as h^{-2} (i.e. a term depending on the mesh size like in the standard mixed wave equation with no convection [26]), a term behaving as $h^{-2}M^2$ and a term behaving as $c_0^{-2}|\nabla\bar{\boldsymbol{u}}|_F^2$ (the second term in (20) can be bounded in terms of the others using Young's inequality). To get a rather simple expression for the parameter fulfilling these requisites, our proposal is to equal every eigenvalue of $\boldsymbol{\tau}^{-1}\boldsymbol{M}\boldsymbol{\tau}^{-1}$ in (22) to a term of the type $[h^{-2}(C_1 + C_2\bar{\boldsymbol{u}}/c_0)^2 + (C_3|\nabla\bar{\boldsymbol{u}}|_F/c_0)^2]$. Direct generalization to the three dimensional case results in

$$\begin{aligned}
\boldsymbol{\tau} &= \begin{pmatrix} \tau_p & 0 & 0 & 0 \\ 0 & \tau_{\boldsymbol{u}} & 0 & 0 \\ 0 & 0 & \tau_{\boldsymbol{u}} & 0 \\ 0 & 0 & 0 & \tau_{\boldsymbol{u}} \end{pmatrix} \text{ with,} \\
\tau_p &= \frac{\rho_0 c_0^2 h}{\left[(c_0 C_1 + C_2|\bar{\boldsymbol{u}}|)^2 + (C_3 h|\nabla\bar{\boldsymbol{u}}|_F)^2\right]^{1/2}}, \\
\tau_{\boldsymbol{u}} &= \frac{h}{\rho_0\left[(c_0 C_1 + C_2|\bar{\boldsymbol{u}}|)^2 + (C_3 h|\nabla\bar{\boldsymbol{u}}|_F)^2\right]^{1/2}},
\end{aligned} \tag{23}$$

where use has been made of the expressions for m_p and $m_{\boldsymbol{u}}$ in (13).

The matrix $\boldsymbol{\tau}$ of stabilization parameters (23) has to be inserted into (12) to get the final stabilized variational formulation proposed in this article. It only remains to find the values of the constants C_1, C_2 and C_3. This will be performed by means of the numerical experiments in Section 4.1. As regards the constants, it should be pointed out that there is a certain tolerance for them, in the sense that one does not necessarily need to get their optimal values as long as they are able to provide

DOI: 10.1002/fld

enough stabilization. For a given mesh size h, the error may be larger or smaller depending on the particular values of the constants, but the slope of the convergence curves will remain unchanged for a wide range of values, which is what matters in fact.

Finally, note that in the case of no mean flow, $\bar{\boldsymbol{u}} = \boldsymbol{0}$, the stabilization parameters for the standard wave equation in mixed form are recovered,

$$\tau_p = Ch\sqrt{\mu_{\boldsymbol{u}}/\mu_p} \quad \tau_{\boldsymbol{u}} = Ch\sqrt{\mu_p/\mu_{\boldsymbol{u}}}, \tag{24}$$

with C standing for a constant [26]. Likewise, if there was no reaction term, $\boldsymbol{S} = \boldsymbol{0}$, the factors $|\nabla\bar{\boldsymbol{u}}|_F^2$ would have not appeared in (23), and we would have recovered analogous stabilization parameters to those found for the standard wave equation in mixed form in an ALE framework [32], or for the equations of wave propagation in shallow waters [31].

3.4. Fully discrete problem

In the aforementioned developments, the time variable has been left continuous. To proceed to the time discretization, we have equally split the time interval $[0\ T]$ into N steps $0 < t^1 < t^2 < \cdots < t^n < \cdots < t^N \equiv T$ with $\Delta t := t^{n+1} - t^n$ denoting the time step size. Hereafter, g^n will stand for the evaluation of a time dependent function $g(t)$ at $t^n = n\Delta t$. Given that we aim at computing the aeroacoustic field only at a few wavelengths from the acoustic source region, a second order backward differentiation formula (BDF2) will prove accurate enough for the time discretization of (12). Was it necessary to compute the acoustic field at several tenth or hundred wavelengths from the source, a less dissipative numerical scheme like the Crank–Nicolson or a higher-order one would prove better. Identifying $\delta_t g^{n+1} := (1/2\Delta t)(3g^{n+1} - 4g^n + g^{n-1})$ allows one to write the time discrete version of (12) as

$$\begin{aligned}&(\boldsymbol{\mu}\delta_t \boldsymbol{U}_h^{n+1}, \boldsymbol{V}_h) + (\boldsymbol{A}_i\partial_i \boldsymbol{U}_h^{n+1}, \boldsymbol{V}_h) + (\boldsymbol{S}\boldsymbol{U}_h^{n+1}, \boldsymbol{V}_h)\\ &\quad + \left(\boldsymbol{\tau}\mathcal{P}[\boldsymbol{F}^{n+1} - (\delta_t \boldsymbol{U}_h^{n+1} + \boldsymbol{A}_i\partial_i \boldsymbol{U}_h^{n+1} + \boldsymbol{S}\boldsymbol{U}_h^{n+1})], -\boldsymbol{A}_i\partial_i \boldsymbol{V}_h + \boldsymbol{S}^\top \boldsymbol{V}_h\right) = (\boldsymbol{F}^{n+1}, \boldsymbol{V}_h).\end{aligned} \tag{25}$$

If we choose the orthogonal subgrid scale approach for the stabilized spatial discretization, it will follow that $\mathcal{P}(\delta_t \boldsymbol{U}_h) = 0$. This is so because U_h belongs to the finite element space, and we are projecting U_h onto the subscale space, which is precisely orthogonal to the latter space (remember that $\mathcal{P} = \boldsymbol{I} - \Pi_h$). The expanded fully discrete problem in time and space that results from accounting for (5) in (25) and that has been implemented for the numerical examples in the forthcoming section reads

$$\begin{aligned}&\frac{1}{\rho_0 c_0^2}(\delta_t p_h^{a\,n+1}, q_h) + \frac{1}{\rho_0 c_0^2}(\bar{\boldsymbol{u}}\cdot\nabla p_h^{a\,n+1}, q_h) + (\nabla\cdot \boldsymbol{u}_h^{a\,n+1}, q_h)\\ &\quad + (\tau_p\mathcal{P}[Q^{n+1} - \frac{1}{\rho_0 c_0^2}\bar{\boldsymbol{u}}\cdot\nabla p_h^{a\,n+1} - \nabla\cdot \boldsymbol{u}_h^{a\,n+1}], -\frac{1}{\rho_0 c_0^2}\bar{\boldsymbol{u}}\cdot\nabla q_h - \nabla\cdot \boldsymbol{v}_h) = (Q^{n+1}, q_h),\end{aligned} \tag{26a}$$

$$\begin{aligned}&\rho_0(\delta_t \boldsymbol{u}_h^{a\,n+1}, \boldsymbol{v}_h) + \rho_0(\bar{\boldsymbol{u}}\cdot\nabla \boldsymbol{u}_h^{a\,n+1}, \boldsymbol{v}_h) + (\nabla p_h^{a\,n+1}, \boldsymbol{v}_h) + \rho_0\left(\boldsymbol{u}_h^{a\,n+1}\cdot\nabla\bar{\boldsymbol{u}}, \boldsymbol{v}_h\right)\\ &\quad + (\tau_{\boldsymbol{u}}\mathcal{P}[-\rho_0\bar{\boldsymbol{u}}\cdot\nabla \boldsymbol{u}_h^{a\,n+1} - \nabla p_h^{a\,n+1} - \rho_0 \boldsymbol{u}_h^{a\,n+1}\cdot\nabla\bar{\boldsymbol{u}}], -\rho_0\bar{\boldsymbol{u}}\cdot\nabla \boldsymbol{v}_h - \nabla q_h + \rho_0 \boldsymbol{v}_h\cdot\nabla\bar{\boldsymbol{u}}) = 0.\end{aligned} \tag{26b}$$

Finally, note that in order to get the final finite element matrix algebraic system, we simply need to substitute $p_h = \sum_{a=1}^{n_p} N_p^a P^a$, and $\boldsymbol{u}_h = \left(\sum_{b=1}^{n_u} N_u^b U_x^b, \sum_{b=1}^{n_u} N_u^b U_y^b, \sum_{b=1}^{n_u} N_u^b U_z^b\right)^\top$, and their analogous for the test functions q_h and $\boldsymbol{v}_h$ in (26). In the preceding expressions, n_p and n_u, respectively, stand for the total number of pressure and velocity nodes in the domain. P^a denote the unknown nodal pressure values and U_x^b, U_y^b and U_z^b the unknown nodal velocity component values. N_p^a are the pressure shape functions, and N_u^b the velocity shape functions, which are taken equal in the forthcoming section on numerical examples.

DOI: 10.1002/fld

4. NUMERICAL EXAMPLES

4.1. Wave propagation in solenoidal convective and shear mean flows

The purpose of this example is twofold. On the one hand, it will allow one to check the influence of the various terms appearing in the APE 3. On the other hand, it will help determining the values of the constants C_1, C_2 and C_3 appearing in the stabilization parameters of (23). Throughout Section 4, the units of all quantities will be those of the SI system and will be not explicitly written.

The example consists of a squared computational domain having dimensions $\Omega = [-100, 100] \times [-100, 100]$. A time varying monopole source of strength,

$$Q = \exp\left[-\ln(2)\frac{x^2 + y^2}{9}\right]\cos(\omega t), \tag{27}$$

has been placed at the origin $(0, 0)$ and generates acoustic waves of angular frequency $\omega = 175$. The propagation of the acoustic waves will be analyzed for different solenoidal mean velocity profiles $\bar{\boldsymbol{u}}$ in the domain. That will reveal the importance of the distinct APE terms in (3). The cases that have been considered are:

- Case A.1: No mean flow, that is, $\bar{\boldsymbol{u}} = \boldsymbol{0}$. In this case, the APE reduce to the standard wave equation in mixed form.
- Case A.2: A constant mean flow with $\bar{\boldsymbol{u}} = (70, 0)$. The APE now reduce to the convective wave equation in mixed form for uniform mean flows.
- Case A.3: A solenoidal shear mean flow with the profile plotted in Figure 1(a) resulting from Equation 28 later. This corresponds to the convective wave equation in mixed form for the case of a non-uniform mean flow. The reaction term $\rho_0 \boldsymbol{u}^a \cdot \nabla \bar{\boldsymbol{u}}$ in (3b) is not taken into account in the simulation.
- Case A.4: The shear mean flow of Case 3 but now considering the full APE in (3) with all non-uniform convective and reaction terms included. This was the benchmark case proposed in [1] to test several APE formulations.

To perform all the simulations for the cases in the aforementioned sections, the computational domain has been discretized with an unstructured mesh of 87 616 triangular elements. This has resulted in approximately nine elements per wavelength. Spurious reflections at the boundaries have been avoided by means of a simple perfectly matched layer (PML) according to the model in [38]. Two additional absorption terms αp and $\alpha^* \boldsymbol{u}$ have been respectively added to the Equations 3a and 3b. α is the attenuation coefficient and $\alpha^* := (\mu_{\boldsymbol{u}}/\mu_p)\alpha$. The attenuation factor is set to zero within the computational domain Ω, while it has been set to $\alpha = 0.0004$ in the absorptive PML surrounding Ω. The width of the PML is 50. With regard to the values of the physical parameters in (3), we have

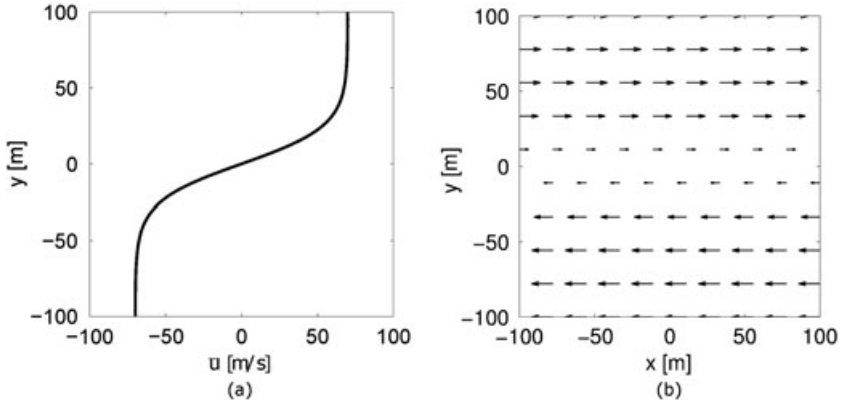

Figure 1. (a) Shear mean velocity profile and (b) resulting vector field for Cases 3 and 4.

DOI: 10.1002/fld

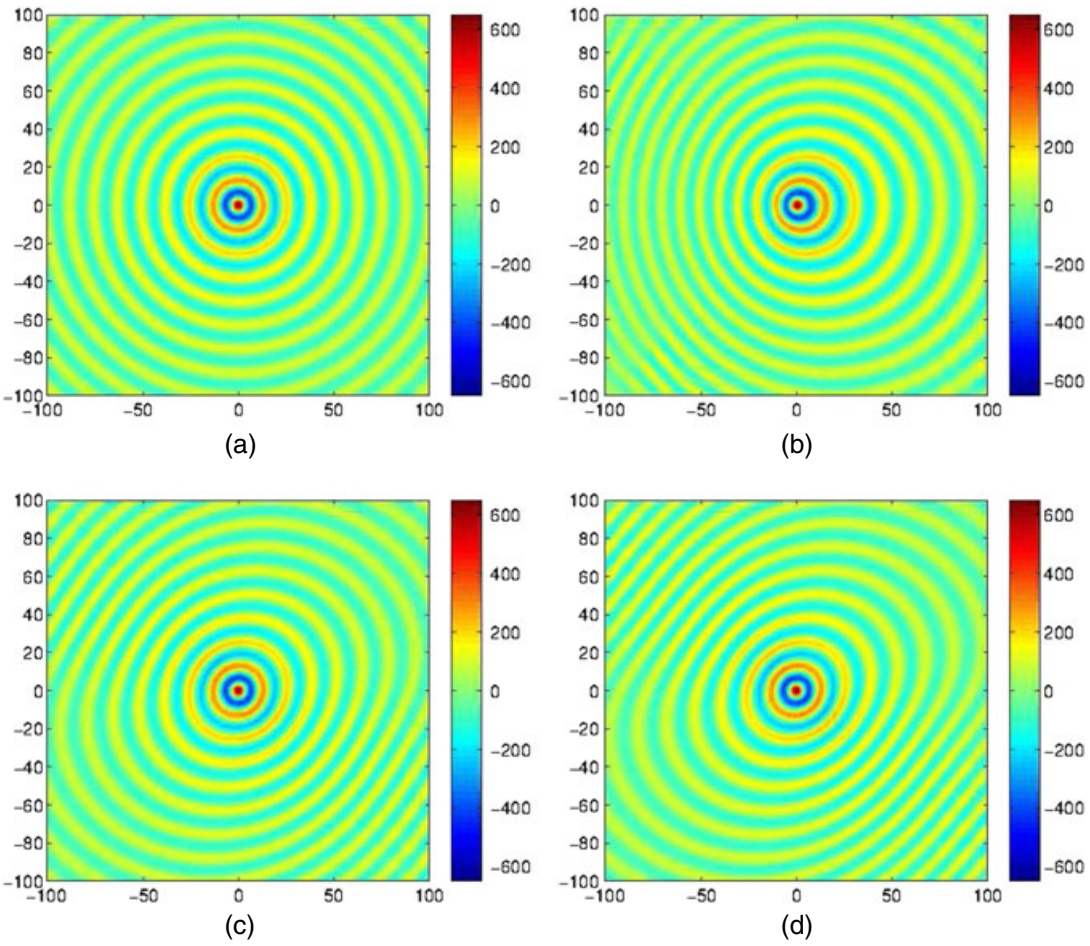

Figure 2. Acoustic pressure contours at time $t = 0.5$. (a) Case A.1: no mean flow. (b) Case A.2: uniform mean flow. (c) Case A.3: shear flow with reaction term excluded. (d) Case A.4: shear flow with reaction term included.

considered an air density of $\rho_0 = 1.14$ and a sound speed of $c_0 = 350$. The shear mean velocity for Cases A.3 and A.4 is defined by (Figure 1(a)),

$$\bar{\boldsymbol{u}}(x, y) = (\bar{U} \tanh(2y/\delta), 0), \tag{28}$$

where $\bar{U}$ is the maximal velocity with value $\bar{U} = 70$ (Mach number $M = 0.2$) and $\delta = 50$ denotes the shear-layer thickness. The resulting mean velocity vector field is plotted in Figure 1(b). In what concerns time evolution, an incremental step of $\Delta t = 7 \times 10^{-4}$ has been chosen to discretize the interval $[0, 0.5]$. Finally, the values $C_1 = 100$, $C_2 = 500$ and $C_3 = 100\,000^2$ have been taken for the constants in the stabilization parameter (see following text for a justification on that choice). It is to be noted that the stabilization parameter dictates the critical time step, $\triangle t_{cr} = \rho_0 \tau_{\boldsymbol{u}} = (\rho_0 c_0^2)^{-1} \tau_p$ of the simulation [39]. This has local values because it depends on the characteristic mesh size, h, as well as on the mean velocity field $\overline{\boldsymbol{u}}$ and its gradient $\nabla \overline{\boldsymbol{u}}$; see (23). If we take the minimum value of $\triangle t_{cr}$ over the computational domain, this results in a CFL number of $C_{CFL} = \triangle t / \triangle t_{cr} \simeq 614$. Instead, if we take an averaged value for $\triangle t_{cr}$ over the domain, we get $C_{CFL} \simeq 74$. This reflects nothing but the well-known fact that when using implicit methods, one can use time step sizes significantly larger than the critical time step.

The resulting acoustic pressure fields for Cases A.1-A.4 have been plotted in Figure 2 at the time instant $t = 0.5$. As observed in Figure 2(a), the wavefronts simply consist of concentric circles propagating outwards for Case A.1, because there is no mean velocity in the domain. We thus recover the expected radiation pattern of a monopole source. When a uniform mean flow is imposed moving

DOI: 10.1002/fld

from left to right in Case A.2 (Figure 2(b)), the front waves travelling upstream get stretched and the wavelength diminishes, whereas the opposite effect takes place for waves propagating downstream. Cases A.3 and A.4 serve to show the importance of taking into account the reaction term in the APE. It is apparent from Figure 2(c) to d that if one was to simulate sound propagation in a shear flow, the use of a convective mixed wave equation with non-uniform velocity (Case A.3) would lead to substantial differences when compared with the predictions made by the full APE (Case A.4). These discrepancies might be better appreciated by plotting the acoustic pressure along the positive x-axis, positive y-axis and along a diagonal cut $x = y$ in the second quadrant of the subfigures Figure 2(c) and (d) (see respectively, Figure 3(a)–(c), where the dashed red line stands for Case A.3 and the blue continuous line for Case A.4).

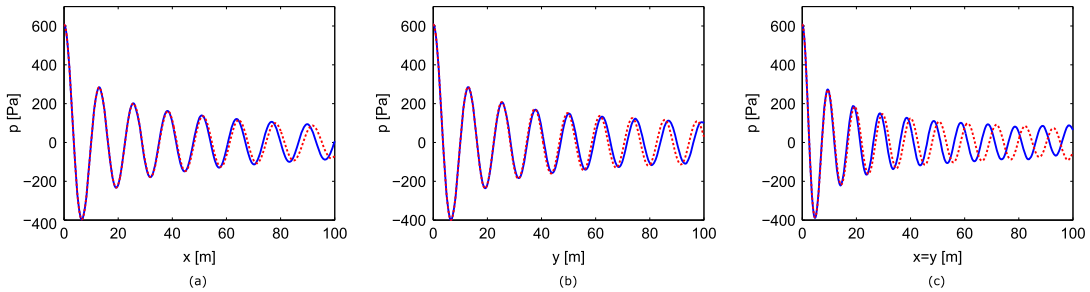

Figure 3. Pressure cuts at $t = 0.5$ corresponding to Figure 2. Case A.3 (dashed red), Case A.4: (continuous blue). (a) x- axis. (b) y-axis. (c) $x = y$.

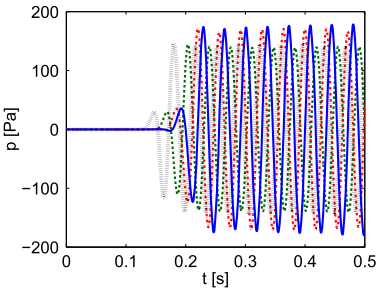

Figure 4. Comparison of the evolution of the pressure at point $(49.6, -34.1)$ for Case A.1 (dashed green), Case A.2 (dotted black), Case A.3 (dot-dashed red) and Case A.4 (continuous blue).

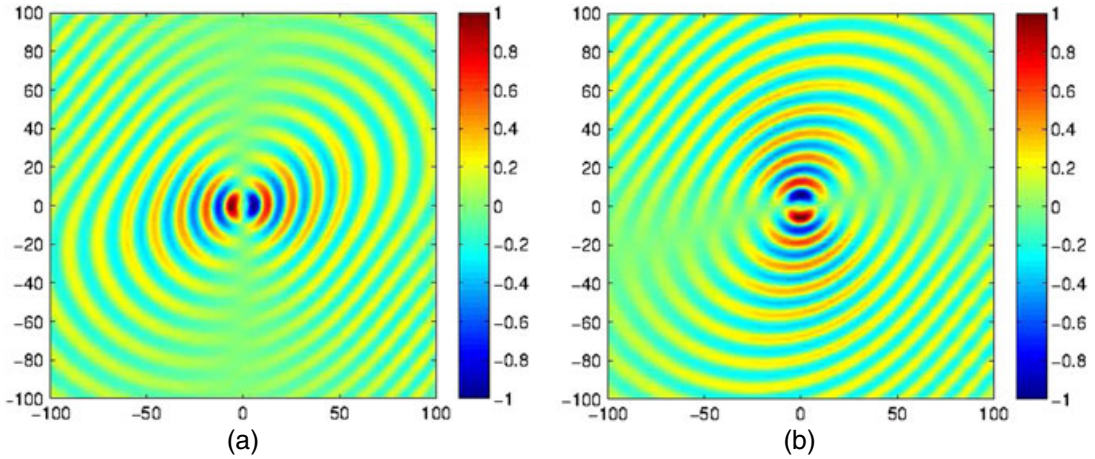

Figure 5. Acoustic velocity contours at time $t = 0.5$ for Case A.4. (a) x-component (b) y-component.

DOI: 10.1002/fld

A plot showing the differences in wave propagation for Cases A.1-A.4 is that of Figure 4. In that figure, we see the time evolution of the acoustic pressure tracked at an arbitrary point A with coordinates $\boldsymbol{x}_A = (49.6, -34.1)$. The differences in amplitudes and phases between cases become again very visible. The zero pressure initial time steps correspond to the time it takes for the first wavefront to travel from the origin, where the source is placed, to A.

Further, it is worthwhile noticing that the APE offer not only the possibility to compute the acoustic pressure but also the acoustic particle velocity. In Figure 5, we show the x and y components of the velocity field at time $t = 0.5$, corresponding to the case A.4. As observed, the values of the velocity components are in clear agreement with the wavefront propagation directions in Figure 2(d).

On the other hand, as mentioned earlier, the second goal of this section is to determine the values of the constants C_1, C_2 and C_3 in the stabilization parameters of (23). The simulations just reported have been carried out following the numerical strategy in Section 3.4, but the values for that constants were yet to be presented. Let us remark that for Case A.1, C_1 is the only constant playing a role given that $\bar{\boldsymbol{u}} = \boldsymbol{0}$. For Cases A.2 and A.3, C_1 and C_2 get involved but not C_3 because the reaction term is not contemplated. Finally, all constants are to be considered in Case A.4.

To find suitable values for the constants, we have compared the results of the stabilized FEM simulations with those from a reference solution computed with a very fine mesh of 420 585 elements. For such a fine mesh, the contribution of the stabilization terms has been checked to be almost negligible. To proceed, we have chosen to compute the relative L^2-error between the computed acoustic pressure p^a and that from the reference solution p^r. This is given by $\varepsilon = \|p^a - p^r\|_2 / \|p^r\|_2$ with $\|p^a - p^r\|_2 = \left[\int_{\Omega_\varepsilon} (p^a - p^r)^2 d\Omega_\varepsilon\right]^{1/2}$. The error is computed in the subdomain $\Omega_\varepsilon \subset \Omega$ so as not to contact the boundaries of Ω and avoid any possible pollution that could stem from the performance of the PML. It is to be noted that we could also have included the relative error for the acoustic velocity in the process, or a weighted combination of relative errors for both, the acoustic velocity and the acoustic pressure. However, given that usually in acoustic problems the latter is the main variable of interest, we have focused on the acoustic pressure.

The value of the C_1 constant was already established in [26], where it appeared in a slightly different form. Given that for $\bar{\boldsymbol{u}} = \boldsymbol{0}$, the results from [26] are to be recovered, we have fixed $C_1 = 100$ to that purpose. The constant C_2 has been selected focusing on Case A.3. For the terms in the denominator of (23) to have similar influence, C_2 should not surpass a value of 2 000. Having a look at the relative error plot in Figure 6(a), we observe that an appropriate value for C_2 is $C_2 = 500$. Once fixed $C_1 = 100$ and $C_2 = 500$, we have resorted to Case A.4 to adjust the constant C_3. This constant should not exceed $150\,000^2$, and as observed from Figure 6(b), the relative error get stabilized for $C_3 \approx 100\,000^2$. As in most stabilized numerical methods, once tuned, the constants $C_1 = 100$, $C_2 = 500$ and $C_3 = 100\,000^2$ are expected to have a rather general character and therefore to apply to many other numerical examples. This is so because the values of the constants

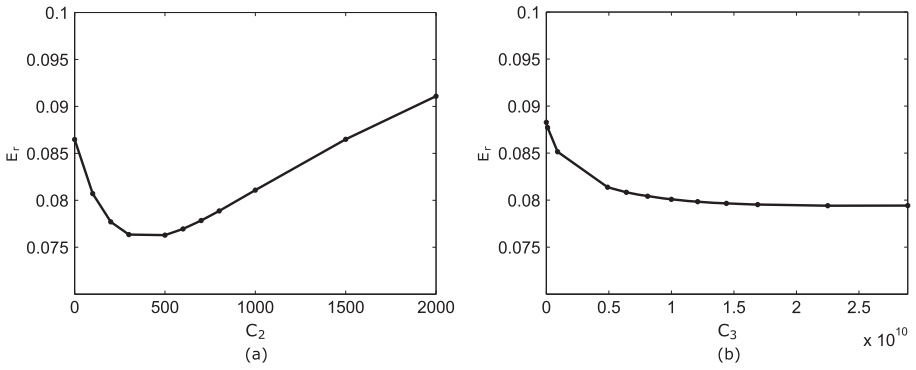

Figure 6. Relative error of the stabilized FEM formulation dependence on the values of the constants in the stabilization matrix. (a) Case 3: relative error dependence on C_2. (b) Case 4: relative error dependence on C_3.

DOI: 10.1002/fld

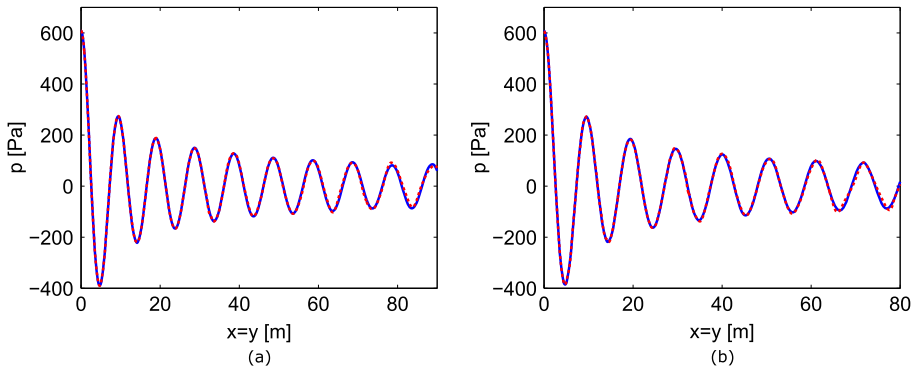

Figure 7. Reference acoustic pressure (blue line) versus stabilized FEM acoustic pressure (red dashed line) for the domain diagonal taking $C_1 = 100$, $C_2 = 500$ and $C_3 = 100\,000^2$. (a) Case A.3. (b) Case A.4.

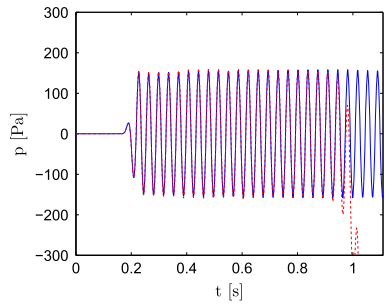

Figure 8. Comparison of the evolution of the pressure at point $(49.6, -34.1)$ for the non-stabilized Galerkin FEM solution (dashed red line) and the stabilized FEM solution (continuous blue line). The Galerkin FEM solution blows up.

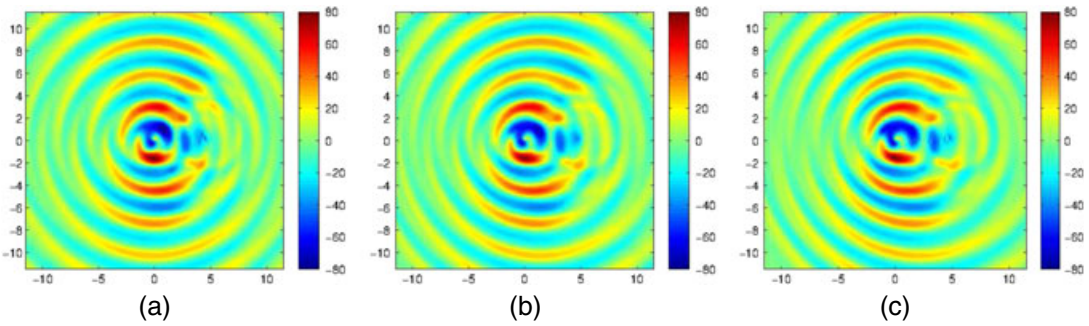

Figure 9. Acoustic pressure contours at time $t = 0.15$. (a) Case C.1. (b) Case C.2. (c) Case C.3.

do not significantly alter the convergence rate of the solutions when refining the computational mesh (e.g. [26, 32] among others). The situation can be thought as being quite analogously to what happens when one changes one computational mesh for another. The overall error of the solution will be different in both meshes, yet the rate of convergence to the reference solution when refining them will be kept unaltered.

To conclude this example, we show the acoustic pressure for the stabilized FEM and reference solutions for the diagonal $x = y$ of the domain in Figure 7. As observed, almost no differences can be appreciated. Yet, had we considered no stabilization at all, the Galerkin FEM solution would have simply blown up in finite time, as appreciated in Figure 8 for the pressure evolution at point $\boldsymbol{x}_A = (49.6, -34.1)$ of the domain.

DOI: 10.1002/fld

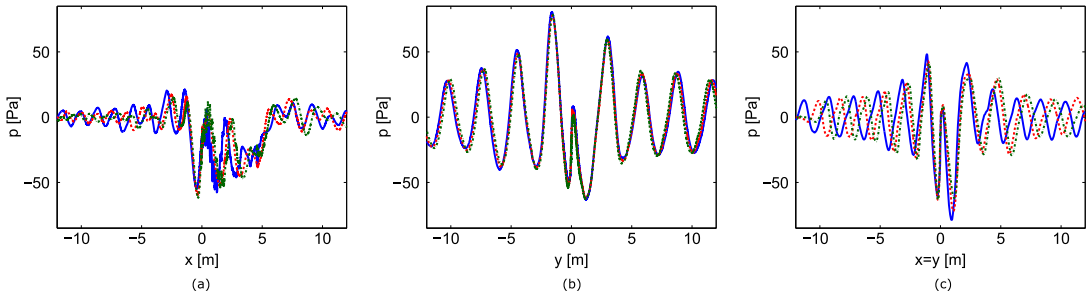

Figure 10. Pressure cuts at $t = 0.15$ corresponding to Figure 9. Case C.1 (continuous blue), Case C.2 (dashed red line), Case C.3 (dashed-dot green line). (a) x- axis. (b) y- axis. (c) $x = y$.

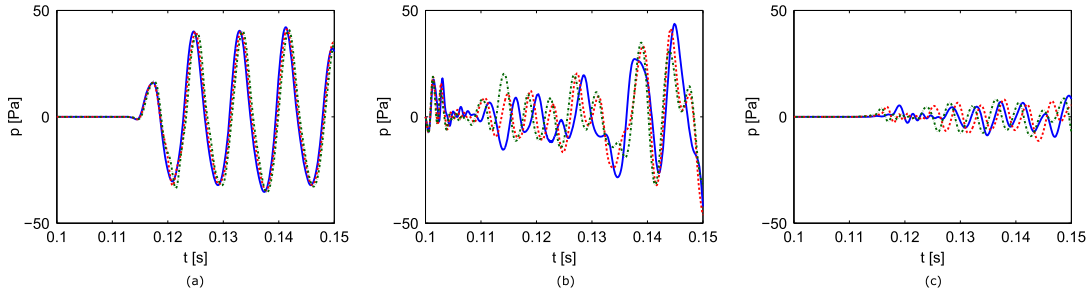

Figure 11. Comparison of the evolution of the pressure for Case C.1 (continuous blue), Case C.2 (dashed red line) and Case C.3 (dashed-dot green line). (a) $\boldsymbol{x}_1 = (-0.2, 5.8)$. (b) $\boldsymbol{x}_2 = (3.1, 0)$. (c) $\boldsymbol{x}_3 = (9, 0)$.

4.2. Aeolian tone generated by a single cylinder

As a final numerical test, we will apply the stabilized FEM approach to the APE, to a more complex situation. This consists in the classical problem of aeolian tone generation by flow past a cylinder. From a physical point of view, the aeroacoustic problem of aeolian tones is well-known and described in literature; see [40, 41] among many others. The problem consists of a flow impinging on a cylinder. For a certain range of Reynolds numbers, a wake of shedding vortices develops past the cylinder inducing lift fluctuating forces on it. That results in the emission of acoustic waves, which exhibit a dipolar radiation pattern at the acoustic far field. For low Mach numbers, the problem can be solved by first performing an incompressible CFD simulation to extract the acoustic source terms and the mean flow, which can then be inserted into the APE (3) to resolve the acoustic field. Our interest in this example is that of showing again the role played by the convection and reaction terms of the APE in the generated aeroacoustic pressure. Consequently, no results will be presented concerning the CFD simulation (they are rather standard and can be found elsewhere, for example, [14, 17]).

In a nutshell and as regards the CFD computation, a two-dimensional cylinder with diameter D=0.1 has been embedded in a squared computational domain of dimensions $\Omega_{CFD} = [-6, 6] \times [-6, 6]$ with an impinging flow velocity, in Cartesian coordinates, of $\boldsymbol{u}_0 = (50, 0)$ (Mach number $M \approx 0.14$ for a sound speed of $c_0 = 350$). The Reynolds number of the problem is $\mathrm{Re} = \rho_0 |\boldsymbol{u}_0| D/\mu = 1000$, where μ denotes the air viscosity. The domain Ω_{CFD} has been meshed with 295 141 linear finite elements. The incompressible Navier–Stokes equations have been solved for a time range of 0.15, using the second order BDF2 time marching scheme with a time step of 9×10^{-5}. The solution has resulted in the generation of a Von Kármán vortex street, with vortices shed at a frequency of 120.

The APE have been resolved in a larger computational domain $\Omega_{ac} = [-12, 12] \times [-12, 12]$, $\Omega_{CFD} \subset \Omega_{ac}$, using an unstructured mesh of 421 804 linear elements. The CFD and acoustic meshes coincide in the domain Ω_{CFD}. The values for the constants in the stabilization parameters found in Section 4.1 have been used for the simulations. Similarly to what has been carried out in that

DOI: 10.1002/fld

subsection, the following three situations have been considered to establish the influence of the various terms in the APE,

- Case C.1: No mean flow; the APE simplifies to the wave equation in mixed form. The sources terms are obtained from the CFD computation.
- Case C.2: The APE using the mean flow and source terms from the CFD computation but neglecting the reaction term. Namely, only non-uniform convection effects are considered.
- Case C.3: The full APE taking into account non-uniform convection and reaction terms.

In Figure 9, we show the acoustic pressure contour levels at the far field for each case. As observed from Figure 9(a), a clear dipole radiation pattern emerges with waves propagating perpendicular to the incident inlet velocity, in Case C.1. However, when convection is taken into account (Case C.2), the wavefronts propagate upstream (Figure 9(b)) as expected [17], the effect being more pronounced if one includes reaction (Case C.3, Figure 9(c)).

The differences in phase and amplitude among Cases C.1–C.3 can be also very clearly appreciated if we plot one-dimensional cuts of the domain in the x, y and diagonal $x = y$ directions (Figure 10(a)–(c)). Again, this is also made apparent when plotting the time evolution of the acoustic pressure at three arbitrary points located at $\boldsymbol{x}_1 = (-0.2, 5.8)$, $\boldsymbol{x}_2 = (3.1, 0)$ and $\boldsymbol{x}_3 = (9, 0)$; see Figure 11(a)–(c).

5. CONCLUSIONS

The FEM solution of wave operators in mixed form requires using tailored finite elements that satisfy the discrete version of the continuous problem inf–sup condition. However, these finite elements are difficult to implement and though valid for the wave equation in mixed form, it has not been tested if they could work well for more complex operators, like the ones in the APE for low Mach numbers.

In this work, we have suggested to circumvent that problem by resorting to a stabilizing variational multiscale FEM formulation for the APE. The APE acoustic pressure and acoustic particle velocity get split into large scales, which can be resolved by the computational mesh and small scales whose influence onto the former has to be modelled. A residual-based model has been chosen for that purpose, the key for its good performance being the design of the matrix of stabilization parameters. The latter has been achieved by setting the small scales equations in the wavenumber domain and using appropriate inequality bounds for its norm as well as for the APE residual. The accomplishment of the proposed strategy has been checked by means of some numerical examples involving wave propagating in solenoidal non-uniform mean flows, involving convection and shear.

APPENDIX A: BOUNDS ON THE ACOUSTIC PERTURBATION OPERATOR SPECTRAL RADIUS

In this appendix, bounds will be given for the spectral radii of the three terms in the RHS of (19). Without loss of generality, results will be derived for the two-dimensional case, their extension to the three dimensional one being straightforward.

Taking into account, the definitions of $\boldsymbol{A}_i$ in (5) and of the scaling matrix $\boldsymbol{M}$ in (13), the matrix in the first term of (19) reads

$$\frac{1}{h^2}k_i^0 k_j^0 \boldsymbol{A}_i^\top \boldsymbol{M} \boldsymbol{A}_j = \frac{1}{h^2}\times \begin{pmatrix} m_{\boldsymbol{u}}|\boldsymbol{k}^0|^2 + \beta_p|\boldsymbol{k}^0\cdot\bar{\boldsymbol{u}}|^2 & \alpha k_1^0(\boldsymbol{k}^0\cdot\bar{\boldsymbol{u}}) & \alpha k_2^0(\boldsymbol{k}^0\cdot\bar{\boldsymbol{u}}) \\ \alpha k_1^0(\boldsymbol{k}^0\cdot\bar{\boldsymbol{u}}) & m_p(k_1^0)^2 + \beta_{\boldsymbol{u}}|\boldsymbol{k}^0\cdot\bar{\boldsymbol{u}}|^2 & k_1^0 k_2^0 m_p \\ \alpha k_2^0(\boldsymbol{k}^0\cdot\bar{\boldsymbol{u}}) & k_1^0 k_2^0 m_p & m_p(k_2^0)^2 + \beta_{\boldsymbol{u}}|\boldsymbol{k}^0\cdot\bar{\boldsymbol{u}}|^2 \end{pmatrix} \tag{A.1}$$

with

$$\alpha \equiv (m_p\mu_p + m_{\boldsymbol{u}}\mu_{\boldsymbol{u}}), \quad \beta_p \equiv m_p\mu_p^2, \quad \beta_{\boldsymbol{u}} \equiv m_{\boldsymbol{u}}\mu_{\boldsymbol{u}}^2. \tag{A.2}$$

DOI: 10.1002/fld

The spectrum of $k_i^0 k_j^0 \boldsymbol{A}_i^\top \boldsymbol{M} \boldsymbol{A}_j$ can be analytically worked out and is given by

$$\mathrm{Spec}_{\boldsymbol{M}^{-1}}(k_i^0 k_j^0 \boldsymbol{A}_i^\top \boldsymbol{M} \boldsymbol{A}_j) = \left\{ \left(\frac{\boldsymbol{k}^0 \cdot \bar{\boldsymbol{u}}}{c_0} + |\boldsymbol{k}^0| \right)^2, \left(\frac{\boldsymbol{k}^0 \cdot \bar{\boldsymbol{u}}}{c_0} \right)^2, \left(\frac{\boldsymbol{k}^0 \cdot \bar{\boldsymbol{u}}}{c_0} - |\boldsymbol{k}^0| \right)^2 \right\}. \tag{A.3}$$

The spectral radius of $\left(\frac{1}{h^2} k_l^0 k_j^0 \boldsymbol{A}_l^\top \boldsymbol{M} \boldsymbol{A}_j \right)$ corresponds to the maximum eigenvalue

$$\rho\left(\frac{1}{h^2} k_l^0 k_j^0 \boldsymbol{A}_l^\top \boldsymbol{M} \boldsymbol{A}_j \right) = \frac{1}{h^2} \left(\frac{\boldsymbol{k}^0 \cdot \bar{\boldsymbol{u}}}{c_0} + |\boldsymbol{k}^0| \right)^2 \equiv \frac{1}{h^2} \left(\frac{C_2 |\bar{\boldsymbol{u}}|}{c_0} + C_1 \right)^2 = \frac{1}{h^2} (C_1 + C_2 M)^2, \tag{A.4}$$

where $M = |\bar{\boldsymbol{u}}|/c_0$ stands for the flow local Mach number (do not confuse the scalar Mach number M with the weighthing matrix $\boldsymbol{M}$). Because $\boldsymbol{k}^0$ is an unknown dimensionless number, we have taken $\boldsymbol{k}^0 \cdot \bar{\boldsymbol{u}} = |\boldsymbol{k}^0||\bar{\boldsymbol{u}}| \cos\theta \equiv C_2 |\bar{\boldsymbol{u}}|$ and $|\boldsymbol{k}^0| \equiv C_1$ in the RHS of (A.4), C_1 and C_2 being dimensionless constants that have to be determined from numerical experiments.

Next, considering the expressions for $\boldsymbol{A}_i$ and $\boldsymbol{S}$ in (5) and for $\boldsymbol{M}$ in (13), we get for the matrix in the second term of (19)

$$2\frac{\mathrm{i}}{h} k_l^0 [\boldsymbol{A}_l \boldsymbol{M} \boldsymbol{S}]_A = \frac{\mathrm{i}}{h} \times \begin{pmatrix} 0 & m_{\boldsymbol{u}} \mu_{\boldsymbol{u}} \boldsymbol{k}^0 \cdot \partial_1 \bar{\boldsymbol{u}} & m_{\boldsymbol{u}} \mu_{\boldsymbol{u}} \boldsymbol{k}^0 \cdot \partial_2 \bar{\boldsymbol{u}} \\ -m_{\boldsymbol{u}} \mu_{\boldsymbol{u}} \boldsymbol{k}^0 \cdot \partial_1 \bar{\boldsymbol{u}} & 0 & -\beta_{\boldsymbol{u}} \boldsymbol{k}^0 \cdot \bar{\boldsymbol{u}} (\partial_1 \bar{u}_2 - \partial_2 \bar{u}_1) \\ -m_{\boldsymbol{u}} \mu_{\boldsymbol{u}} \boldsymbol{k}^0 \cdot \partial_2 \bar{\boldsymbol{u}} & \beta_{\boldsymbol{u}} \boldsymbol{k}^0 \cdot \bar{\boldsymbol{u}} (\partial_1 \bar{u}_2 - \partial_2 \bar{u}_1) & 0 \end{pmatrix}. \tag{A.5}$$

The spectrum of this matrix is given by

$$\mathrm{Spec}_{\boldsymbol{M}^{-1}} \left(2\frac{\mathrm{i}}{h} k_l^0 [\boldsymbol{A}_l \boldsymbol{M} \boldsymbol{S}]_A \right) = \left\{ \frac{1}{h} \left[(c^2 + b^2) + m_{\boldsymbol{u}} d^2 \right]^{1/2}, 0, -\frac{1}{h} \left[(c^2 + b^2) + m_{\boldsymbol{u}} d^2 \right]^{1/2} \right\}, \tag{A.6}$$

with

$$\begin{aligned} c^2 + b^2 &= \frac{1}{c_0^2} \left[(\boldsymbol{k}^0 \cdot \partial_1 \bar{\boldsymbol{u}})^2 + (\boldsymbol{k}^0 \cdot \partial_2 \bar{\boldsymbol{u}})^2 \right] \leqslant \frac{1}{c_0^2} |\boldsymbol{k}^0|^2 |\nabla \bar{\boldsymbol{u}}|_F^2, \\ m_{\boldsymbol{u}}^2 d^2 &= m_{\boldsymbol{u}}^2 \beta_{\boldsymbol{u}} (\boldsymbol{k}^0 \cdot \bar{\boldsymbol{u}})^2 (\partial_1 \bar{u}_2 - \partial_2 \bar{u}_1)^2 \leqslant \frac{1}{c_0^4} |\boldsymbol{k}^0|^2 |\bar{\boldsymbol{u}}|^2 (\partial_1 \bar{u}_2 - \partial_2 \bar{u}_1)^2 \leqslant \frac{1}{c_0^2} |\boldsymbol{k}^0|^2 M^2 |\nabla \bar{\boldsymbol{u}}|_F^2, \end{aligned} \tag{A.7}$$

$|\boldsymbol{B}|_F$ denoting the Frobenius norm of an arbitrary matrix $\boldsymbol{B}$. It follows that

$$c^2 + b^2 + m_{\boldsymbol{u}}^2 d^2 \leqslant \frac{1}{c_0^2} |\boldsymbol{k}^0|^2 |\nabla \bar{\boldsymbol{u}}|_F^2 (1 + M^2) \leqslant \frac{2}{c_0^2} |\boldsymbol{k}^0|^2 |\nabla \bar{\boldsymbol{u}}|_F^2, \tag{A.8}$$

where we have considered that we are dealing with low Mach number flows and consequently $M << 1$. The aforementioned results allow one to bound the spectral radius of $2\frac{\mathrm{i}}{h} k_l^0 [\boldsymbol{A}_l \boldsymbol{M} \boldsymbol{S}]_A$ by

$$\rho\left(2\frac{\mathrm{i}}{h} k_l^0 [\boldsymbol{A}_l \boldsymbol{M} \boldsymbol{S}]_A \right) \leqslant \frac{1}{h} \frac{C_3}{c_0} |\nabla \bar{\boldsymbol{u}}|_F, \tag{A.9}$$

C_3 denoting a dimensionless real constant.

Finally, the matrix in the third term of (19) reads

$$\boldsymbol{S}^\top \boldsymbol{M} \boldsymbol{S} = \begin{pmatrix} 0 & 0 & 0 \\ 0 & \beta_{\boldsymbol{u}} |\partial_1 \bar{\boldsymbol{u}}|^2 & \beta_{\boldsymbol{u}} \partial_1 \bar{\boldsymbol{u}} \cdot \partial_2 \bar{\boldsymbol{u}} \\ 0 & \beta_{\boldsymbol{u}} \partial_1 \bar{\boldsymbol{u}} \cdot \partial_2 \bar{\boldsymbol{u}} & \beta_{\boldsymbol{u}} |\partial_2 \bar{\boldsymbol{u}}|^2 \end{pmatrix}, \tag{A.10}$$

DOI: 10.1002/fld

with spectrum

$$\mathrm{Spec}_{\boldsymbol{M}^{-1}}(\boldsymbol{S}^{\top}\boldsymbol{M}\boldsymbol{S}) = \left\{\frac{m_{\boldsymbol{u}}}{2}\left[(e+f)+\sqrt{(e-f)^2+4g^2}, 0, \frac{m_{\boldsymbol{u}}}{2}\left[(e+f)-\sqrt{(e-f)^2+4g^2}\right\}\right.\right., \tag{A.11}$$

where

$$\begin{aligned}(e+f) &= \beta_{\boldsymbol{u}}\left[(\partial_1\bar{\boldsymbol{u}})^2+(\partial_2\bar{\boldsymbol{u}})^2\right] \leqslant \beta_{\boldsymbol{u}}|\nabla\bar{\boldsymbol{u}}|_F^2,\\ (e-f)^2 &= \beta_{\boldsymbol{u}}^2\left[|\partial_1\bar{\boldsymbol{u}}|^2-|\partial_2\bar{\boldsymbol{u}}|^2\right]^2 \leqslant \beta_{\boldsymbol{u}}^2|\nabla\bar{\boldsymbol{u}}|_F^4,\\ 4g^2 &= 4\beta_{\boldsymbol{u}}^2(\partial_1\bar{\boldsymbol{u}}\cdot\partial_2\bar{\boldsymbol{u}})^2 \leqslant 4\beta_{\boldsymbol{u}}^2|\partial_1\bar{\boldsymbol{u}}|^2|\partial_2\bar{\boldsymbol{u}}|^2 \leqslant 4\beta_{\boldsymbol{u}}^2|\nabla\bar{\boldsymbol{u}}|_F^4.\end{aligned} \tag{A.12}$$

Therefore, the spectral radius of $\boldsymbol{S}^{\top}\boldsymbol{M}\boldsymbol{S}$ can be bounded as

$$\rho(\boldsymbol{S}^{\top}\boldsymbol{M}\boldsymbol{S}) \leqslant C_4 m_{\boldsymbol{u}}\beta_{\boldsymbol{u}}|\nabla\bar{\boldsymbol{u}}|_F^2 = \frac{C_4}{c_0^2}|\nabla\bar{\boldsymbol{u}}|_F^2, \tag{A.13}$$

with C_4 denoting a large enough dimensionless real constant to be found again from numerical experiments.

From (A.4), (A.9) and (A.13), we get

$$\begin{aligned}&\rho\left(\frac{1}{h^2}k_l^0k_j^0\boldsymbol{A}_l^{\top}\boldsymbol{M}\boldsymbol{A}_j\right)+\rho\left(2\frac{\mathrm{i}}{h}k_l^0[\boldsymbol{A}_l\boldsymbol{M}\boldsymbol{S}]_A\right)+\rho(\boldsymbol{S}^{\top}\boldsymbol{M}\boldsymbol{S})\\ &\leqslant \frac{1}{h^2}(C_1+C_2M)^2+\frac{1}{h}\frac{C_3}{c_0}|\nabla\bar{\boldsymbol{u}}|_F+\frac{C_4}{c_0^2}|\nabla\bar{\boldsymbol{u}}|_F^2.\end{aligned} \tag{A.14}$$

ACKNOWLEDGEMENTS

This work is supported by EU-FET grant EUNISON 308874. The third author would like also to acknowledge the Generalitat de Catalunya (SUR/ECO) for the predoctoral FI Grant no. 2015 FI-B 00227. The fifth author acknowledges the support received from the Catalan Government through the ICREA Acadèmia Research Program.

REFERENCES

1. Ewert R, Schröder W. Acoustic perturbation equations based on flow decomposition via source filtering. *Journal of Computational Physics* 2003; **188**(2):365–398.
2. Lighthill MJ. On sound generated aerodynamically I. general theory. *Proceedings of the Royal Society of London Series A* 1952; **211**(1107):564–587.
3. Powell A. Theory of vortex sound. *Journal of the Acoustical Society of America* 1964; **36**(1):177–195.
4. Howe M. The generation of sound by aerodynamic sources in an inhomogeneous steady flow. *Journal of Fluid Mechanics* 1975; **67**(03):597–610.
5. Möhring W. On vortex sound at low Mach number. *Journal of Fluid Mechanics* 1978; **85**(04):685–691.
6. Curle N. The influence of solid boundaries upon aerodynamic sound. *Proceedings of the Royal Society of London Series A* 1955; **231**(1187):505–514.
7. Williams JF, Hawkings DL. Sound generation by turbulence and surfaces in arbitrary motion. *Philosophical Transactions of the Royal Society A* 1969; **264**(1151):321–342.
8. Bailly C, Bogey C, Gloerfelt X. Some useful hybrid approaches for predicting aerodynamic noise. *Comptes Rendus Mécanique* 2005; **333**(9):666–675.
9. Lilley G. On the noise radiated from a turbulent high speed jet. In *Computational Aeroacoustics*, Hardin JC, Hussaini MY (eds). Springer Verlag, 1993.
10. Goldstein M. A generalized acoustic analogy. *Journal of Fluid Mechanics* 2003; **488**:315–333.
11. Bailly C, Bogey C. Contributions of computational aeroacoustics to jet noise research and prediction. *International Journal of Fluid Dynamics* 2004; **18**(6):481–491.
12. Slimon SA, Soteriou MC, Davis DW. Development of computational aeroacoustics equations for subsonic flows using a mach number expansion approach. *Journal of Computational Physics* 2000; **159**(2):377–406.
13. Oberai AA, Roknaldin F, R Hughes TJ. Computation of trailing-edge noise due to turbulent flow over an airfoil. *AIAA Journal* 2002; **40**(11):2206–2216.
14. Guasch O, Codina R. Computational aeroacoustics of viscous low speed flows using subgrid scale finite element methods. *Journal of Computational Acoustics* 2009; **17**(3):309–330.

DOI: 10.1002/fld

15. Kaltenbacher M, Escobar M, Becker S, Ali I. Numerical simulation of flow-induced noise using LES/SAS and lighthill's acoustic analogy. *International Journal for Numerical Methods in Fluids* 2010; **63**(9):1103–1122.
16. Baiges J, Codina R. A variational multiscale method with subscales on the element boundaries for the Helmholtz equation. *International Journal for Numerical Methods in Engineering* 2013; **93**(6):664–684.
17. Guasch O, Codina R. An algebraic subgrid scale finite element method for the convected Helmholtz equation in two dimensions with applications in aeroacoustics. *Computer Methods in Applied Mechanics and Engineering* 2007; **196**(45–48):4672–4689.
18. Hueppe A, Kaltenbacher M. Spectral finite elements for computational aeroacoustics using acoustic perturbation equations. *Journal of Computational Acoustics* 2012; **20**(02):1240005.
19. Harari I. A survey of finite element methods for time-harmonic acoustics. *Computer Methods in Applied Mechanics and Engineering* 2006; **195**(13):1594–1607.
20. Bécache E, Joly P, Tsogka C. An analysis of new mixed finite elements for the approximation of wave propagation problems. *SIAM Journal on Numerical Analysis* 2000; **37**(4):1053–1084.
21. Bécache E, Joly P, Tsogka C. Fictitious domains, mixed finite elements and perfectly matched layers for 2-D elastic wave propagation. *Journal of Computational Acoustics* 2001; **9**(3):1175–1201.
22. Bécache E, Joly P, Tsogka C. A new family of mixed finite elements for the linear elastodynamic problem. *SIAM Journal on Numerical Analysis* 2002; **39**(6):2109–2132.
23. Hughes T. Multiscale phenomena: Green's function, the dirichlet-to-neumann formulation, subgrid scale models, bubbles and the origins of stabilized formulations. *Computer Methods in Applied Mechanics and Engineering* 1995; **127**:387–401.
24. Hughes T, Feijóo G, Mazzei L, Quincy J. The variational multiscale method, a paradigm for computational mechanics. *Computer Methods in Applied Mechanics and Engineering* 1998; **166**:3–24.
25. Codina R. Stabilized finite element approximation of transient incompressible flows using orthogonal subscales. *Computer Methods in Applied Mechanics and Engineering* 2002; **191**:4295–4321.
26. Codina R. Finite element approximation of the hyperbolic wave equation in mixed form. *Computer Methods in Applied Mechanics and Engineering* 2008; **197**(13–16):1305–1322.
27. Badia S, Codina R, Espinoza H. Stability, convergence and accuracy of stabilized finite elements methods for the wave equation in mixed form. *SIAM Journal on Numerical Analysis* 2014; **52**:1729–1752.
28. Langtangen HP, Pedersen G. Computational models for weakly dispersive nonlinear water waves. *Computer Methods in Applied Mechanics and Engineering* 1998; **160**(3-4):337–358.
29. Walkley M, Brezins M. A finite element method for the two-dimensional extended Boussinesq equations. *International Journal for Numerical Methods in Fluids* 2002; **39**(10):865–885.
30. Hauke G. A symmetric formulation for computing transient shallow water flows. *Computer Methods in Applied Mechanics and Engineering* 1998; **163**(1-4):111–122.
31. Codina R, González-Ondina J, Díaz-Hernández G, Principe J. Finite element approximation of the modified Boussinesq equations using a stabilized formulation. *International Journal for Numerical Methods in Fluids* 2008; **57**(9):1249–1268.
32. Guasch O, Arnela M, Codina R, Espinoza H. A stabilized finite element method for the mixed wave equation in an ALE framework with application to diphthong production. *Acta Acustica united with Acustica* 2016; **102**(1):94–106.
33. Rao PP, Morris P. A stabilized finite element method for the mixed wave equation in an ALE framework with application to diphthong production. *AIAA Journal* 2006; **44**(7):1643–1652.
34. Iob A, Arina R, Schipani C. Frequency-domain linearized Euler model for turbomachinery noise radiation through engine exhaust. *AIAA Journal* 2010; **48**(4):848–858.
35. Codina R, Principe J, Guasch O, Badia S. Time dependent subscsales in the stabilized finite element approximation of incompressible flow problems. *Computer Methods in Applied Mechanics and Engineering* 2007; **196**(21–24): 2413–2430.
36. Codina R, Principe J. Dynamic subscales in the finite element approximation of thermally coupled incompressible flows. *nternational Journal for Numerical Methods in Fluids* 2007; **54**:707–730.
37. Ávila M, Codina R, Principe J. Large eddy simulation of low mach number flows using a dynamical and nonlinear finite element subgrid scale model. *Computers & Fluids* 2008; **57**(9):1249–1268.
38. Takemoto H, Mokhtari P, Kitamura T. Acoustic analysis of the vocal tract during vowel production by finite-difference time-domain method. *Journal of the Acoustical Society of America* 2010; **128**(6):3724–3738.
39. Codina R, Zienkiewicz O. CBS versus GLS stabilization of the incompressible Navier–Stokes equations and the role of the time step as stabilization parameter. *Computer Methods in Applied Mechanics and Engineering* 2002; **18**: 99–112.
40. Howe MS. *Acoustics of Fluid-structure Interactions*. Cambridge university press, 1998.
41. Drazin P. *Introduction to Hydrodynamic Stability*. Cambridge University Press: Cambridge Texts in Applied Mathematics, 2002.

DOI: 10.1002/fld